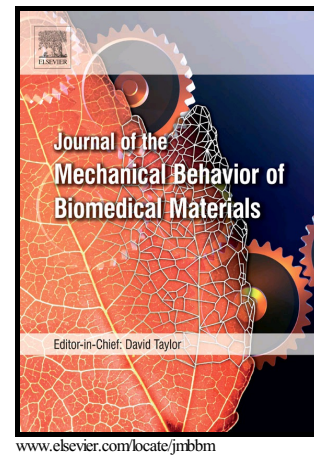# Author's Accepted Manuscript

An Investigation of the Viscoelastic Properties and the Actin Cytoskeletal Structure of Triple Negative Breast Cancer Cells

Jingjie Hu, Yuxiao Zhou, John D. Obayemi, Jing Du, Winston O. Soboyejo

Cite this article as: Jingjie Hu, Yuxiao Zhou, John D. Obayemi, Jing Du and Winston O. Soboyejo, An Investigation of the Viscoelastic Properties and the Actin Cytoskeletal Structure of Triple Negative Breast Cancer Cells, *Journal of the Mechanical Behavior of Biomedical Materials,* https://doi.org/10.1016/j.jmbbm.2018.05.038

This is a PDF file of an unedited manuscript that has been accepted for publication. As a service to our customers we are providing this early version of the manuscript. The manuscript will undergo copyediting, typesetting, and review of the resulting galley proof before it is published in its final citable form. Please note that during the production process errors may be discovered which could affect the content, and all legal disclaimers that apply to the journal pertain.

An Investigation of the Viscoelastic Properties and the Actin Cytoskeletal Structure of Triple Negative Breast Cancer Cells

Jingjie Hu[a,b], Yuxiao Zhou[c], John D. Obayemi[d,e], Jing Du[c], Winston O. Soboyejo[a,b,d,e*]

[a] Department of Mechanical and Aerospace Engineering, Princeton University, Olden Street, Princeton, NJ 08544, USA

[b] Princeton Institute of Science and Technology of Materials (PRISM), Princeton University, 70 Prospect Street, Princeton, NJ 08544, USA

[c] Department of Mechanical and Nuclear Engineering, Penn State University, 136B Leonhard Building, University Park, PA 16802, USA

[d] Department of Mechanical Engineering, Higgins Lab, 100 Institute Road, Worcester Polytechnic Institute (WPI), Worcester, MA 01609, USA

[e] Department of Biomedical Engineering, Gateway Park Life Sciences Center, 60 Prescott Street, Worcester Polytechnic Institute (WPI), Worcester, MA 01605, USA

Corresponding author. Winston O. Soboyejo: Address: Atwater Kent 128, 100 Institute Road, Worcester, MA 01609, USA. Phone: 508-831-4694; Fax: 508-831-5680. wsoboyejo@wpi.edu

Abstract

An improved understanding of the evolution of cell structure and viscoelasticity with cancer malignancy could enable the development of a new generation of biomarkers and methods for cancer diagnosis. Hence, in this study, we present the viscoelastic properties (moduli and viscosities) and the actin cytoskeletal structures of triple negative breast cancer (TNBC) cells with different metastatic potential. These include: MCF-10A normal breast cells (studied as a control); MDA-MB-468 cells (less metastatic TNBC cells), and MDA-MB-231 cells (highly metastatic TNBC cells). A combination of shear assay and digital imaging correlation (DIC) techniques is used to measure the local viscoelastic properties of live breast cells subjected to constant shear stress. The local moduli and viscosities of the nuclei and cytoplasm are characterized using a generalized Maxwell model, which is used to determine the time-dependent creep responses of cells. The nuclei are shown to be stiffer and more viscous than the cytoplasms of the normal breast cells and TNBC cells. The MCF-10A normal breast cells are found to be twice as stiff as the less metastatic MDA-MB-468 breast cancer cells and over ten times stiffer than the highly metastatic MDA-MB-231 breast cancer cells. Similar trends are also observed in the viscosities of the nuclei and the cytoplasms. The measured differences in cell viscoelastic properties are also associated with significant changes in the cell cytoskeletal structure, which is studied using confocal fluorescence microscopy. This reveals significant differences in the levels of actin expression and organization in TNBC cells as they become highly metastatic. Our results suggest that the shear assay measurements of cell viscoelastic properties may be used as effective biomarkers for TNBC diagnosis and screening.

Graphical abstract
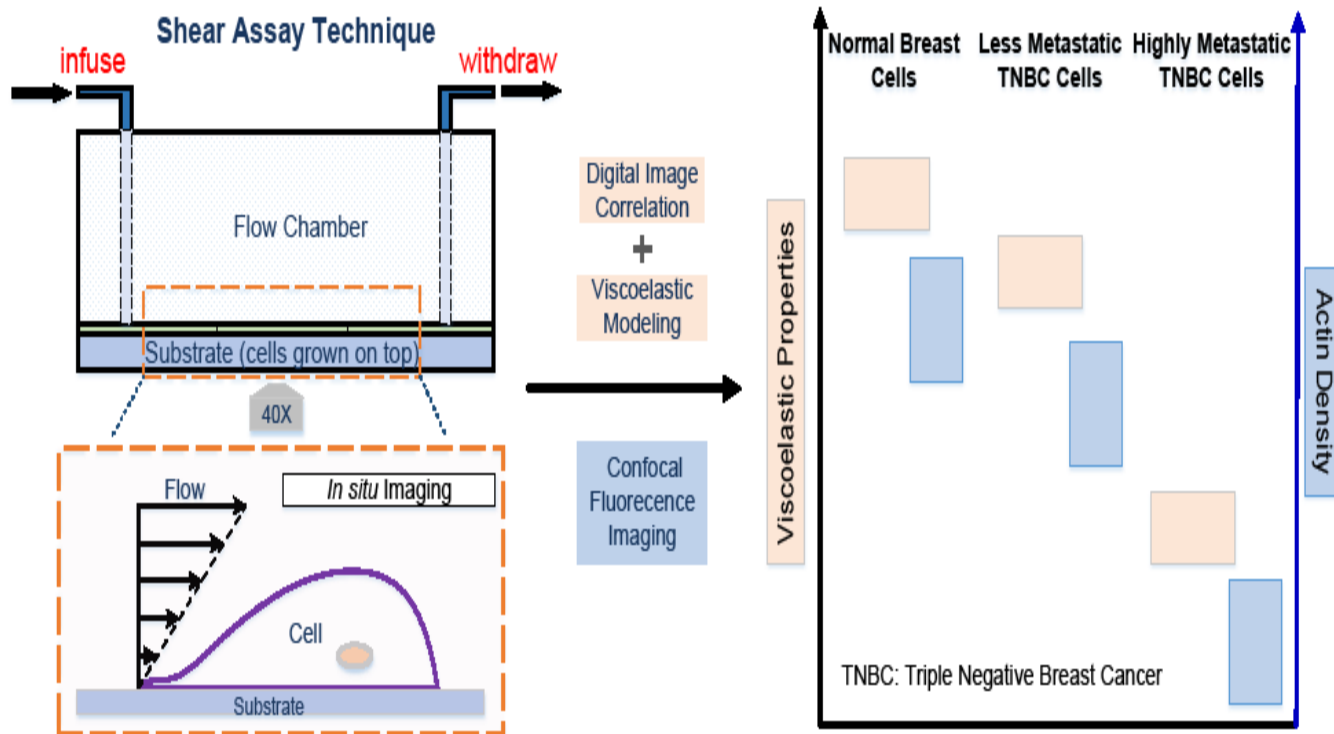
1. Introduction

Changes in cell viscoelastic properties have been associated with the onset and progression of certain human diseases [1-6]. In the case of cancer, significant changes in cell stiffness and viscosity have been reported in cancer cells, compared to their healthy counterparts [7-10]. The alterations in the stiffness of cancer cells have also been related to differences of cytoskeletal structure [10-14] and the degree of malignancy [15-17]. Hence, measurements of single cell viscoelastic properties can provide experimental and clinical approaches for the diagnosis and tracking of cancer progression.

Effective biomarkers are needed, especially in the case of triple negative breast cancer (TNBC), which is estrogen-receptor (ER) negative, progesterone-receptor (PR) negative and HER2-receptor negative [18-20]. Hence, the lack of these prognostic and predictive biomarkers leads to poorer prognosis than other breast cancer subtypes [21]. TNBC accounts for approximately 15% of all breast cancers [21], while its overall survival rate is 78.5% [22]. Also, the unproportionally high recurrence and mortality rates [21] can be attributed to the limitations in current breast cancer screening techniques. For instance, TNBC may exhibit benign features in mammography and ultrasound screening [23-25], resulting in the misinterpretation of images or delay in the diagnosis of the disease. It is, therefore, essential to develop new biomarkers and approaches for

2

the detection of TNBC [26, 27]. This will be explored in this paper using measurements of viscoelastic properties of TNBC cells with different malignancy/metastatic conditions, which cannot be captured by current imaging technique.

A number of techniques have been developed for the measurement of cell viscoelastic properties [5, 28, 29]. These include: atomic force microscopy (AFM) [12, 13, 16, 30-32]; magnetic twisting cytometry [33-35]; micropipette aspiration [36-38]; optical trapping [4, 39, 40]; micro patterned substrate [41-43] and embedded particle tracking [44-46]. Although these methods have been widely used, they can also lead to induced effects that can affect intracellular structure. These include: the effects of indentation depth, complex tip geometries and substrate stiffening in AFM [47, 48]; laser-induced heating and photodamage during optical trapping [40, 49], and complex stress states associated with micropipette aspiration [38, 50]. Such undesired effects can often result in significant uncertainties in the measurements of cell viscoelasticity [5, 28, 29].

Hence, in our prior work [51], we have used a shear assay technique as an alternative approach for the measurement of cell viscoelastic properties. It uses a combination of a parallel flow chamber device and digital image correlation (DIC) techniques to study the deformation of biological cells in fluidic environments that are comparable to cell physiological environments. In particular, the parallel flow chamber device has been used extensively to study cell adhesion [52-56], drug effects [57-59] and cell physiological changes [60, 61]. However, there is only one prior paper (from our group) [51] on the use of the shear assay technique for the measurement of the cell viscoelasticity of human osteosarcoma cells [51].

Furthermore, it has been shown that cancer metastasis is usually accompanied with the remodeling of the actin cytoskeletal structure [12, 13, 16]. Cellular cytoskeleton is made up of microtubules, actin microfilaments and intermediate filaments, while actin filaments are considered as the main determinants for cell rigidity [62-64]. Studies have suggested that the reduced rigidity of cancer cells is related to the loss of actin filaments when cells mutate from benign to cancerous states [65-67]. Although a number of research groups [12, 13, 32] have used fluorescence staining and imaging to demonstrate the evolution of actin structure during the breast cancer metastasis, several studies [12, 13, 32] have presented two-dimensional images that do not sufficiently characterize the three-dimensional structures of the actin cytoskeleton. There is, therefore, a need to study the evolution of the three-dimensional structures of the actin filaments in cancer cells with different malignancy. Such changes may also be related to the shear assay measurement of cell viscoelasticity.

Hence, in this study, we use a shear assay system, in parallel with a confocal microscope, to study the evolution of cell viscoelastic properties (modulus, viscosity and relaxation time) and the actin cytoskeletal structures TNBC cells. This is done using highly metastatic MDA-MB-231 TNBC cells, less metastatic MDA-MB-468 TNBC cells and normal MCF-10A breast cells (as control). We show that the viscoelastic properties of TNBC cells can be used as effective biomarkers for the characterization of tumor evolution. The measurements of cell viscoelastic

properties are also correlated with changes in the underlying of the actin cytoskeletal structure with different cell metastatic potential.

2. Materials and Methods

2.1. Sample Preparation

The MDA-MB-231 (Cat # HTB-26) and MDA-MB-468 (Cat # HTB-132) breast cancer cells were grown, respectively, in L-15 base media, supplemented with 100 I.U./ml penicillin/100 µg/ml streptomycin and 10% FBS (all obtained from American Type Culture Collection (ATCC), Manassas, VA, USA). Both types of breast cancer cells were incubated at 37°C under normal atmospheric pressure.

The MCF-10A normal breast cell line (provided by Prof. Yibin Kang of Princeton University, USA) were cultured at 37°C in 5% CO_2 atmosphere in the following medium: DMEM/F12 medium (Invitrogen, Carlsbad, CA, USA) supplemented with 5% horse serum (Invitrogen, Carlsbad, CA, USA), 30 ng/ml murine epidermal growth factor (PeproTech, Rocky Hill, NJ, USA), 0.5 µg/ml hydrocortisone (Sigma-Aldrich, St. Louis, MO, USA), 100 ng/ml cholera toxin (Sigma-Aldrich, St. Louis, MO, USA), 10 µg/ml insulin (Sigma-Aldrich, St. Louis, MO, USA), 1% Penicillin-Streptomycin (Invitrogen, Carlsbad, CA, USA), and 0.2% amphotericin (Gemini Bio Products, West Sacramento, CA, USA).

The cells were cultured in 35 mm Falcon dishes (Corning Inc., Corning, NY, USA) for 48 hours to ensure their proper attachment and spreading on the substrate. The cells were seeded with a density of 5000 cells per petri dish, respectively. The low seeding densities allowed that the distances between individual cells were greater than the individual cell dimensions. This ensured that the observed single cell deformation was not significantly affected by the surrounding neighboring cells. Prior to shear assay experiments, the cell culture medium was aspirated and the cells were rinsed with Dulbecco Phosphate-Buffered Saline (DPBS) (Thermo Fisher Scientific, Waltham, MA, USA) that was pre-warmed in a water bath at 37°C.

2.2. Shear Assay Technique

In this work, we used a modified shear assay technique, developed previously in our group by Cao et al. [51], to study the viscoelastic properties of normal/cancerous breast cells. The system setup is shown in Fig. 1. Briefly, the apparatus consists of a syringe pump (for liquid delivery) and a parallel flow chamber (for generation of wall shear stress). The dual syringe pump (Fig. 1A) (Harvard Apparatus, Holliston, MA, USA) supplies continuous flow, of which the infusion and withdraw flow rates are kept identical. The parallel plate flow chamber (Fig. 1B), obtained from Glycotech Corporation (Gaithersburg, MD, USA), is designed to use with 35 mm Falcon petri dishes. The flows are connected with supplied tubing and connectors to form a complete infusion and withdraw loop.

4

The flow profile was designed and controlled using a combination of flow rate, flow path geometry and the type of flow (Fig. 1). The flow rates were typically varied between 3-5 mL/min. A rubber gasket (Fig. 1C) was used as an interlayer between the flow chamber and the cell substrate, to create flow path. In particular, its middle rectangular opening channel (height and width) dimensions determined the flow profile. Serum-free culture media were used to prevent non-specific extracellular matrix protein binding. In selected cases, methyl cellulose (Sigma Aldrich, St. Louis, MO, USA), which is non-toxic and non-allergenic [51], was added into the serum free culture medium to increase the viscosity of the cell culture medium and thus, the wall shear stress. Specifically, 3.5 wt% methyl cellulose (viscosity $= 0.16\ Pa \cdot s$) was added to cell culture medium in the cases of both MCF-10A and MDA-MB-468 cells, while no cellulose was introduced to medium in the case for MDA-MB-231 cells (viscosity $= 0.002\ Pa \cdot s$). The viscosity of the mixture was then measured using a rheometer (Anton Paar, Ashland, VA, USA) operating at 37°C (Fig. 2). This is because less shear stress is needed to deform MDA-MB-231 cells. The shear rates are kept identical to be $2500 s^{-1}$.

The flow medium viscosity was adjusted to optimize the flow parameters for cell deformation and detachment in the shear assay system. The rubber gasket thickness and channel dimensions were also selected, together with the performed flow rate, to ensure that the Reynolds number, $Re = \frac{\rho Q}{(w+h)\mu}$, in the rectangular flow channel ($Re < 1$) was in the laminar flow regime ($Re < 100$) [68]. Here, ρ and μ represents fluid density and viscosity, respectively; Q is the flow rate; w and h are the channel width and channel height, respectively. The shear stress was calculated from the following relation (Fig. 1E) [51, 52], which gives

$$\sigma = \frac{6\mu Q}{wh^2} \qquad (1)$$

Furthermore, the rubber gasket provides vacuum suction through the peripheral holes to hold the flow chamber in place with respect to the substrate.

Before the shear assay experiment, the flow medium was pre-heated to 37°C in a water bath. The tubing was then pre-flushed with the medium to evacuate any residual bubbles in the flow line. This was done to avoid the disturbance to the cells during the experiments. In addition, the connected tubing were immersed in a 37°C water bath to maintain the temperature of the fluid that was delivered to the cells. The cells were then subjected to uniform flow and velocities that were used to control the wall shear stresses.

During each shear assay experiment, the typical cell deformation and detachment event usually occurred within a period of approximately three minutes for all three types of cells that were used in this study. The cellular response (to liquid flow) in the flow chamber was monitored *in situ* using an optical microscope (Nikon Instruments Inc., Melville, NY, USA) and a video camera (INFINITY2-1R, Lumenera Corporation, Ottawa, ON, Canada) (Fig. 1D). Specifically, the 35 mm Falcon dish, containing the gasket and flow chamber, was placed on the sample stage of an inverted microscope, equipped with a bright field camera. A 40 X objective was used to find cell

candidates (isolated single cells, without adjacent neighbors) to monitor their movements and detachment from the substrate.

During the shear assay experiments, the cells were located on the left-hand side of the field of view (while flow direction was from left to right) to ensure that the cell displacement events were easy to observe. The deformation of nuclei and cytoplasms were recorded with the *in situ* video camera. The recordings were stopped when the cells detached (flipped away) from the substrate. The videos were captured at 24 fps with a 1392×1040 pixel resolution. The individual frames were then extracted for digital image correlation analysis.

2.3. Digital Image Correlation (DIC)

After the background images were digitally masked, digital image correlation (DIC) was performed on the cell images using DaVis software (LaVision, Goettingen, Germany). DIC tracks the movement of the naturally patterned structures (nuclei and cytoplasms) by locating each block of pixels (subset) of the reference image in the deformed images. A subset size of 31×31 pixels ($5.5 \ \mu m \times 5.5 \ \mu m$) and a step size of 8 pixels ($1.4 \ \mu m$) were chosen for the optimized correlation value. Step size defines the distance that each subset is shifted before performing next correlation.

Two consecutive images in the time series were used as the reference image and deformed image, respectively, to accommodate larger deformations in this study. The results were then superposed over time to obtain the cell deformation at each time point. Strain values were calculated based on the derivatives of the displacement fields. The maximum shear strain over time was extracted and analyzed using MATLAB R2015b (The MathWorks, Inc., Natick, MA, USA) for approximately 30 locations in the nucleus and in the cytoplasm within each cell.

2.4. Immunofluorescence Assay and Confocal Microscopy Imaging

In this study, immunofluorescence staining of cytoskeleton structure was performed on MCF-10A normal breast cells, MDA-MB-468 TNBC cells and MDA-MB-231 TNBC cells. This was used to characterize the distribution and relative density of actin cytoskeletal structure. The three cell lines were cultured separately on No. 1.5 coverslips inside the sterile 60×15 mm Falcon cell culture Petri dishes in their respective medium. After 48 hours, the cells were fixed with 4% high-grade paraformaldehyde (4% in 0.1 M PBS, Electron Microscopy Science, Hatfield, PA, USA). After 10 minutes, the paraformaldehyde was aspirated and was followed by three rinses with PBS. The cell samples were then permeabilized, each with 1 mL 0.1% solution of Triton X-100 (Life Technologies Corporation, Carlsbad, CA, USA) for 5 minutes. This was followed by three rinses with PBS as well.

Subsequently, the cell samples were incubated in PBS with 1% BSA (Signma-Aldrich, St. Louis, MO, USA) at room temperature for 30 minutes to block non-specific binding. The samples were then rinsed thrice with PBS, before incubating the cells for 30 minutes in the dark at room temperature (25°C) with 200 μL of 100 nM acti-stain 488 phalloidin (Cytoskeleton, Inc., Denver,

USA) in PBS. This was followed by three rinses with PBS. Finally, the cell nuclei were stained with 200 μl of 100 nM DAPI for 2 minutes, followed by three rinses with PBS. The resulting samples were drained and mounted on clean glass slides, with a drop of FluoroGuard Reagent (Bio-Rad Laboratories, Hercules, CA, USA) as the mounting medium.

2.5. Confocal Laser Scanning Microscopy

The stained cell samples were imaged using a 40X oil immersion objective and a 63x oil immersion objective, respectively, with an inverted Leica SP5 Point Scanning Confocal Microscope (Leica Microsystems, Heidelberg, Germany). An argon gas laser with a wavelength of 488 nm was used to detect 488 phalloidin fluorophore (actin cytoskeleton) and a 405-nm diode laser was used for DAPI fluorophore (nucleus). The cells were imaged starting and finishing the stack at least 1 μm below and above the cell height limits. The images were collected at 0.25-μm intervals in the z-direction under identical system parameter settings.

2.6. Fluorescence Imaging Analysis

The average fluorescence intensity, I (fluorescence per unit volume), of actin filaments was estimated for each cell line using the three-dimensional confocal image stacks. This was done to compare the actin expression levels in three different types of breast cells. The three-dimensional image visualization and interpretation were carried out using ImageJ (ImageJ software package, NIH, Bethesda, MD, USA). Each three-dimensional confocal image stack was divided into individual slices using ImageJ and every stack contains approximately 30 to 60 slices. The total amount of fluorescence within each slice was measured according to published protocols [69, 70].

Each image was analyzed manually to ensure the accuracy of the cell peripheral outline. This was done for all slices within a stack, in order to measure I within individual cells. The total fluorescence was calculated by combing integrated actin levels in every plane within a single cell. The total volume was estimated by stacking consecutive slices in z-stack from confocal images at steps of 0.25 μm. The fluorescence intensity was then obtained by dividing the total fluorescence by the cell volume. Ten individual cells per cell line were analyzed for their fluorescence intensities. The mean and standard deviation values were then reported.

2.7. Statistical Analysis

The raw data were analyzed using one-way ANOVA. The statistical differences between the means were considered significant at $p < 0.05$.

3. Viscoelastic Modeling

In this study, cells (both nucleus and cytoplasm regimes) undergoing creep are subjected to constant stress. The primary creep region is studied using a generalized Maxwell viscoelastic model (Fig. 3). The model describes time-dependent strain due to viscoelastic effects. In addition, the constitutive relationship is shown in Eq. 2. The top dashpot is represented by $(\sigma/\eta_1)t$,

accounting for the viscous behavior. The second term on the right stands for the Voigt component that represents the elasticity [51]. The effective cellular viscosity is, therefore, denoted by the value obtained from the top dashpot, η_1, and the characteristic time τ is given by η_2/E.

$$\varepsilon = \left(\frac{\sigma}{\eta_1}\right) t + \frac{\sigma}{E}\left(1 - \exp\left(-\frac{t}{\tau}\right)\right) \qquad\qquad (2)$$

Eq. 2 was used to fit the strain-time data obtained in the primary creep region. This was done by using the "Curve Fitting" Toolbox in MATLAB R2015b (The MathWorks, Inc., Natick, MA, USA). The three fitting parameters ($\sigma/\eta_1, \sigma/E$ and E/η_2) were adjusted to yield high R^2 values ($90\% < R^2 < 100\%$). Characteristic viscoelastic properties were then extracted from the fitting parameters. In particular, E represents the shear modulus that characterizes cell elastic properties, η_1 is the viscosity that corresponds to cell resistance to deformation under shear stress and τ is the relaxation time which is a characteristic time-scale for cell to reach equilibrium state after the removal of external stress. The mean and the standard deviation values are reported for cytoplasm and nucleus regions, respectively.

4. Results

4.1. Cell Deformation under Continuous Fluid Flow

A representative set of analyzed images by DIC is represented in Fig. 4. The image series in Fig. 4 illustrate the deformation stages for a MDA-MB-231 highly metastatic TNBC cell under continuous flow. The cell was initially resistant to the shear stress ($\sigma = 10\ Pa$). This was followed by a period of observable deformation prior to cell detachment from the plastic substrate. The constant wall shear stress, σ, at the onset of cell detachment was determined to be 410 Pa for both MCF-10A normal breast cells and MDA-MB-468 less metastatic breast cancer cells (Fig. 5), and 10 Pa for MDA-MB-231 highly metastatic breast cancer cells, based on Eq. 1. Hence, much lower shear stresses were needed to detach the MDA-MB-231 cells from the plastic substrate.

The cell deformation (Fig. 4A) and the strain distributions (Fig. 4B) obtained using DIC are presented in Fig. 4. Within the first second, the strain values at the same location modulates with small variations (less than 0.20 strain) comparing to the later stage. Afterwards, it is clear that the discrete meshes distort and fluctuate more at the periphery of the cell, indicating its relative large displacement/strain compared to the middle portion (refer to red arrows). The more distorted grids are consistent with higher levels of cellular deformation and larger maximum shear strains.

The local maximum shear strains are plotted against time for various locations within the same MDA-MB-231 breast cancer cell, which is subjected to constant wall shear stress of 10 Pa, in Fig. 4C. The plots show that the different locations all undergo creep deformation. Specifically, Fig. 4C presents the time-dependent strain response at six separate locations (three for cytoplasm and three for nucleus), which are denoted in Fig. 4A. In addition, distinct three-stage creep behavior is revealed in nucleus (Fig. 4D): the primary regime was associated with the initial elastic

deformation, during which the slope first increase rapidly before decreasing; the second stage exhibited a relatively small slope, while in the last stage, the strain increased rapidly with respect to time until cell detachment occurred from the substrate. To this end, only the primary stage is used for model fitting to evaluate viscoelastic properties, since cell will experience detachment towards later stage, which may involve coupling effect from cell-substrate adhesion. It is clear that the time-dependent strains in the nuclei were much lower than those of the cytoplasms. Furthermore, larger variations in creep rates were observed in the cytoplasms compared to those in the nuclei. This suggests that the nuclei were more homogeneous than the cytoplasms. Similar phenomena were observed on the nuclei and cytoplasms of the MDA-MB-468 cells (less metastatic TNBC cells) (Figs. 5A and 5B) and the MCF-10A cells (normal breast cell) (Figs. 5C and 5D).

4.2. Measurements of Cell Viscoelastic Properties

The observed strain-time creep response was well characterized using the three-element generalized Maxwell model (Fig. 3) presented in Section 3. Fig. 6 presents the moduli (E), viscosities (η_1), and characteristic relaxation times (τ) obtained from individual cells (no adjacent neighbors) for all three types of breast cells. Distinct viscoelastic properties were observed across the three cell types. Specifically, there is a noticeable downward trend in the moduli and viscosities of the healthy cells, compared to those of the cancer cells (MDA-MB-468 and MDA-MB-231). These results are demonstrated in the floating bar charts (Fig. 6) in which we present averages, standard deviations, medians, ranges of measured data (25% to 75%), as well as the raw data, which are displayed to the left of the bars.

The cell elasticity was characterized by the shear modulus (Fig. 6A). The modulus of MCF-10A normal breast cells ($7966 \pm 2536\ Pa$ and $3598 \pm 1511\ Pa$ for nucleus and cytoplasm, respectively) was over ten times greater than that of MDA-MB-231 highly metastatic breast cancer cells ($622 \pm 340\ Pa$ and $261 \pm 148\ Pa$ for the nucleus and cytoplasm, respectively). Furthermore, the less metastatic MDA-MB-468 breast cancer cells had moduli ($5632 \pm 2089\ Pa$ and $3334 \pm 1764\ Pa$ for the nucleus and cytoplasm) that were approximately one and half time less than those of the normal breast cells. In all cell lines, the nucleus was much stiffer than the cytoplasm region ($p < 0.05$). The coefficients of variation were also higher for the cytoplasm region than that of nucleus (Fig. 6A).

In addition, there is a significant statistical difference in E between MCF-10A normal breast cells and MDA-MB-231 highly metastatic TNBC cells ($p < 0.05$ for both nucleus and cytoplasm), and MDA-MB-468 less metastatic breast cells and MDA-MB-231 highly metastatic TNBC cells ($p < 0.05$ for both nucleus and cytoplasm). While the difference between MCF-10A and MDA-MB-468 was not statistically significant ($p = 0.21$ for cytoplasm and $p < 0.05$ for nucleus), the three cell lines can be differentiated using the modulus, E ($p < 0.05$ for both nucleus and cytoplasm).

Similar trends were observed in the viscosities obtained for all three cell lines (Fig. 6B). Specifically, a fifteen-fold decrease in viscosity was observed when cells are becoming highly

9

metastatic (MDA-MB-231) ($325 \pm 234 \, Pa \cdot s$ and $215 \pm 135 \, Pa \cdot s$ for nucleus and cytoplasm) comparing to that of normal MCF-10A breast cells ($6868 \pm 3095 \, Pa \cdot s$ and $3598 \pm 1511 \, Pa \cdot s$ for nucleus and cytoplasm, respectively). The average viscosity values also show a 20% reduction in the less metastatic MDA-MB-468 cancer cells ($5616 \pm 2887 \, Pa \cdot s$ and $3390 \pm 2106 \, Pa \cdot s$), compared to their healthy counterparts. The distribution of viscosities was greater in the cytoplasm compared to that in the nucleus ($p < 0.05$).

In addition, there was a significant statistical difference in η obtained for MCF-10A normal breast cells and highly metastatic MDA-MB-231 TNBC cells ($p < 0.05$ for both nucleus and cytoplasm). Large differences in η were also observed between MDA-MB-468 less metastatic breast cells and MDA-MB-231 highly metastatic TNBC cells ($p < 0.05$ for both nucleus and cytoplasm). However, η values obtained for the MCF-10A and MDA-MB-468 cells were not significantly different ($p = 0.27$ for cytoplasm and $p < 0.05$ for nucleus). The three cell lines can be readily distinguished by their values, η ($p < 0.05$ for both nucleus and cytoplasm).

The ranges of the moduli and viscosities were also investigated. The output of MDA-MB-468 less metastatic cancer cells situated well within the output range of MCF-10A normal cells. A significant overlap in the values of these two parameters was observed for both the nucleus and cytoplasm. However, there is a clear gap between the upper bound values obtained for highly metastatic MDA-MB-231 cancer cells and the lower bound values obtained for MCF-10A normal cells. This indicates a clear difference in viscoelastic properties between the two. It is also interesting to observe that the lower bound output of MDA-MB-468 less metastatic breast cancer cells coincides well with the upper bound values of highly metastatic MDA-MB-231 breast cancer cells. This suggests that the difference in mechanical properties is detectable from one malignancy state to another.

Lastly, the characteristic relaxation times are identical within the uncertainty for all three types of cell lines but are statistically different ($p < 0.05$) (Fig. 6C). In particular, the MDA-MB-231 breast cancer cells have overall smallest relaxation times ($0.3 \pm 0.3 \, s$). The average relaxation time decreases by approximately 50% from the less metastatic ($0.6 \pm 0.4 \, s$) to highly metastatic cancer cells ($0.3 \pm 0.3 \, s$) ($p < 0.05$). However, the relaxation times cannot distinguish the normal cells ($0.5 \pm 0.3 \, s$) from the less metastatic breast cancer cells ($0.6 \pm 0.4 \, s$) ($p < 0.38$ for cytoplasm and $p = 0.07$ for nucleus). It is important to note that the relaxation time has a wide range and large standard deviation for all three types of cells.

4.3. Three-dimensional Immunofluorescence Characterization

Fig. 7 shows confocal immunofluorescence images, revealing noticeable changes in the actin cytoskeletal structure in TNBC cells with different maligancy. All the cells were stained and imaged under identical conditions, in which the actin cytoskeleton was stained green, while the nucleus was stained blue. The representative z-stack orthogonal projections clearly show that the MCF-10A normal breast cell (Fig. 7A) exhibits the highest amount of green fluorescence, indicating a denser and thicker actin filament network. The network contains either well-aligned long fibers or short filaments that are distributed across the cell (Fig. 7A).

In contrast, Fig. 7B reveals that the MDA-MB-468 cells still have long actin filaments, while they are thinner, loosely organized, and distributed mainly at the basal section. Although, the upper cellular sections have lower levels of actin, there is a noticeable presence of actin in the cortex regions. Lastly, Fig. 7C shows that the level of actin expression in highly metastatic MDA-MB-231 cells is the least. Furthermore, a less well-defined actin network is observed in the MDA-MB-231 cells, consisting of short and randomly oriented branches in the perinuclear region. Moreover, actins are absent in the apical section of these highly metastatic cancer cells.

Fig. 8 represents the actin density structures at different cell heights for individual cell shown in Fig. 7. These were obtained from the reconstructed 3D stack images. The results show that the MCF-10A normal breast cell had actin filaments that were distributed across the whole cell. Its actin structure was also more closely spaced than that in two types of breast cancer cells at similar positions. Furthermore, both types of breast cancer cells expressed actin filaments towards the basal sections of the cells (not the apical sections), while the less metastatic MDA-MB-468 TNBC cells contained higher levels of actins than the highly metastatic MDA-MB-231 TNBC cells. It is also interesting to notice that the MCF-10A normal breast cells had the highest peak heights (~10 μm), followed by MDA-MB-468 breast cancer cells that had intermediate peak heights (~6 μm), and the MDA-MB-231 breast cancer cells that had the lowest peak heights (4 μm). The latter were rather flat and spread onto the substrate.

Since all the cells were stained and imaged under identical conditions, we focus on qualitative comparison across three types of breast cells, rather than the exact amount of actin. Therefore, it is important to note that the fluorescence has arbitrary units (a.u.). The relative comparison of volume density of actin filaments between three cells is shown in Fig. 9, demonstrating a clear downward trend as the cells evolve from healthy to tumorigenic states. A 75% reduction of actin concentration was observed as the breast cancer cells transitions from benign ($165 \pm 35\ a.u.$) to tumorigenic states ($41 \pm 9\ a.u.$). In addition, a 65% decrease in actin filament expression was observed as breast cancer evolves from less metastatic ($117 \pm 20\ a.u.$) to highly metastatic stage ($41 \pm 9\ a.u.$). The findings correlate well with the trends observed in modulus and viscosity shown in Fig. 6A and Fig. 6B, respectively.

5. Discussion

In this study, we strive to unravel the correlations between cell viscoelasticity and the underlying actin cytoskeletal structure. The results suggest that the cell viscosity and moduli decrease with the increased metastatic potential from normal breast cells to tumorigenic states. The observed decrease in cancer cell viscosities and moduli are also associated with lower levels of actin expression and less organized actin cytoskeletal structure.

5.1. Creep Behavior of Cells

Since biological cells are viscoelastic [5], their time-dependent material behavior can be characterized using spring-dashpot models [71]. In particular, when cells are loaded under

constant stress, they undergo creep deformation. This leads to a multi-stage creep behavior (Figs. 4 and 5). The primary creep behavior can be well characterized by a three-element Maxwell model [51, 72] (Fig. 3), in which the top dashpot η_1 captures the permanent creep phenomena.

Our results reveal that the generalized Maxwell model successfully differentiates cancer cells at different stages (Figs. 4 and 5). This suggests that the model may serve as an encouraging mechanical analog. Furthermore, the Maxwell circuit offers good fit to the creep data (Figs. 4E, 5C and 5F). It also provides a comprehensive output of viscoelastic properties, which include the modulus, viscosity, as well as the characteristic relaxation time (Fig. 6). Beyond this, the long-time flow behavior of TNBC cells, which is related to intercellular network rearrangement and microstructural reorganization, is well represented by the model.

While the different nuclei appear to have similar deformation profiles, the regions in the cytoplasm exhibit significant differences in creep rates from point to point (Figs. 4C, 5A and 5D). It is also clear that the cytoplasm undergoes higher levels of deformation than the nucleus. The variations in the strain rates obtained in the cytoplasm are attributed to differences between the numerous organelles within the cytoplasm. In contrast, the more uniform structure of the nucleus results in smaller variations in the measured strain rates that were obtained in this study.

In addition, there is a need to consider the deformation of adhesion proteins (e.g. integrins) during the shear flow. Both experimental and theoretical studies [73-79] indicate that integrins are approximately 10 nm above the cell membrane in their inactive conformation (e.g. bending). The integrins can also extend up to 25 nm upwards from the cell surface at their active conformation (e.g. fully extended). These results suggest that there is a maximum of ~15 nm of extension in integrins. While such small length change cannot be resolved in current setup, as the best possible resolution can be achieved is ideally ~20 nm (tenth of the pixel size, which is ~200 nm) for our system. However, such resolution can only be reached under the perfect condition (e.g. optimum contrast and camera setting etc., which is not applicable in current study). Therefore, cell deformation mainly dominates the shape change.

Furthermore, Wang *et al.* [80] have demonstrated a theoretical study which correlates the strain at the vicinity of focal attachment (FA) sites to the tissue-loading amplitudes induced by flow. For instance, this study demonstrates that small tissue stress of 0.1 MPa at 30 Hz leads to axial strain of 1.5 % and radial strain of 0.2 % around the FAs. While a loading of 20 MPa at 30 Hz on tissue leads to 12 % of axial strain around the FAs. In addition, tissue strains are shown to be amplified 10-fold or more at the cellular level. From Ref. [80], we estimate that 10 Pa of cell loading (~1 Pa of tissue loading) would lead to a maximum of ~0.1 % strain around FAs, in spite of loading frequency. The total strain measured from DIC at initial stage of cell deformation (Fig. 4) is then estimated to be at least 10 times more than the predicted strain around the FAs. This again suggests that the strain field around FA is negligible compared to the strain experienced by the cell body.

Finally in this section, it is interesting to note that the protein mechanics is of great importance in the understanding of cell mechanobiology. This can be studied experimentally using fluorescence resonance energy transfer (FRET) microscopy, which is a powerful technique that enables nanoscale probing between two molecules in the study of live protein dynamics [77]. Combining FRET with parallel flow chamber would permit us to study integrin deformation under shear flow [77]. This should be considered for future work.

5.2. Correlations between Viscoelastic Properties and Cancer Malignancy

Distinct viscoelastic properties were obtained for two types of breast cancer cells and the normal breast cells. Our results suggest that there are significant differences in the elastic moduli and viscosities of the normal breast cells and the highly metastatic breast cancer cells (over ten-fold differences in magnitude), while the differences between the normal states and the less metastatic states were lower (the viscosities of the breast cancer cells one and half times lower) (Fig. 6). One remarkable observation is that highly metastatic cancer cells (MDA-MB-231) are more compliant and less viscous than normal breast cells (MCF-10A). Hence, the lowest levels of cell moduli and viscosities are associated with metastatic cancer cells.

In particular, cells with greatest decrease in stiffness and viscosity are the most aggressive and show the greatest potential for metastasis. This is consistent with the results from prior studies that use cell mechanics to grade cancer malignancy [10, 12, 13, 16, 17, 30]. The compliant and less viscous cancer cells are also easier to squeeze into tiny capillaries and confining pores with much smaller diameters [81-83]. This facilitates their migration to distant sites, where they can induce metastases in other organs, such as the lungs and the bones in the case of TNBC [84].

It is important to note that most of the measured moduli and viscosity values of MDA-MB-468 (less metastatic TNBC) cells overlaps with those of MCF-10A healthy cells. This is attributed to the relatively less metastatic potential of MDA-MB-468 cells. Since such less malignant TNBC is not associated with significant reorganization of the actin cytoskeletal structure (Fig. 7B), the cell moduli and viscosities are less affected (Figs. 6A and 6B). On the contrary, the significant changes in the cytoskeletal structure of the metastatic MDA-MB-231 TNBC cells (Fig. 7C) result in very significant reductions of cell moduli and viscosities (Figs. 6A and 6B).

The relaxation times obtained for the three cell lines were quite close, as shown in Fig. 6C. However, a slightly lower relaxation time was obtained for the MDA-MB-231 highly metastatic breast cancer cells (0.3 ± 0.3 s for nucleus and 0.4 ± 0.3 s for cytoplasm). The relaxation time corresponds to the time requested for induced strains to drop from their initial values, ε_0, to ε_0/e, where e is a mathematical constant that approximately equals to 2.71. Also, the highly metastatic cells are the most deformable, in turn suggesting that the time for the cell to recover is less than the other two types of cells, since the reorganization of the internal structure happens faster. However, the relaxation time of the less metastatic cells (MDA-MB-468) is comparable to that of the normal MCF-10A cells (Fig. 6C). This suggests that the cell relaxation time on its own is not a sensitive measure of tumorigenic stage during the early stages of cancer.

The observed trends, as well as the measured moduli of obtained modulus and viscosities, in three breast cell lines are in good agreement with those reported in the literature [12, 13, 85-87]. However, it is interesting to note that, the values obtained from this study are generally overall higher than those obtained from AFM techniques [12, 13, 32]. For example, Calzado-Martin *et al.* [12] have reported that in the case of low indentation loading-rates (1 Hz), MCF-10A has an average elastic modulus of 0.7 ± 0.3 kPa, while MDA-MB-231 breast cancer cells have an

elastic modulus of $0.3 \pm 0.1\ kPa$. In addition, Guck *et al.* [88] used an optical stretcher, in parallel with microfluidic channel, to demonstrate that optical deformability directly correlated with cell viscoelastic properties, which can serve as a sensitive indicator for disease monitoring. This study was performed in the context of breast cancer cells with different degree of malignancy, including MCF-10A normal breast cells and MDA-MB-231 TNBC cells.

Since the elastic moduli obtained from AFM depend on tip geometry, indentation depth and loading rate, the AFM measurements of cell moduli are associated with the indentation of the cell cortex and the soft membrane. Therefore, the local stiffness within the cell body is unable to be accurately assessed. In particular, breast cancer cells contain more actin fibers in basal sections [12, 13] (Figs. 7A and 7B). The local viscoelasticity resulting from these actin filaments is not accessible by AFM. In contrast, the combined shear assay and DIC method measures much wider variations in cell mechanical properties over the full cell structure, in which larger variations in actin cytoskeleton are observed in three dimensions (Figs. 6 and 7).

5.3. Correlations between Viscoelastic Properties and Actin Cytoskeletal Structures

Finally, it is important to discuss the effects of the actin cytoskeletal structures on cell viscoelasticity (Figs. 6-9). Among the subcomponents in cytoskeleton (actin, microtubules and intermediate filament), studies have shown that actin is the major determinant of cell elasticity while microtubules do not significantly influence cell rigidity [89-92]. Hence, in this work, a strong effort was made to reveal the underlying cytoskeletal structures by the staining of the actin filaments (Figs. 7-9). Fig. 7 reveals relatively dense actin networks in the normal MCF-10A breast cells and less metastatic MDA-MB-468 TNBC cells, respectively. While in the highly metastatic state (MDA-MB-231 cells), there is a significant loss of actin concentration and less well-developed actin structures. This suggests that the much lower moduli and viscosities of the MDA-MB-231 cells are associated with the lower densities of actin cytoskeletal structures in the highly metastatic TNBC cells.

In addition to actin cytoskeletal structure, the differences between less metastatic MDA-MB-468 and highly metastatic MDA-MB-231 cells in active transport mechanisms and their remodeling capabilities were investigated by Goldstein *et al.* through intracellular particle tracking [93]. Their results revealed that the internal motion of both types of cells are actually driven by fluctuating microtubules and their associated molecular motors while the main mechanisms and actin participation differ in these two cases [93]. Specifically, the active transport in highly metastatic MDA-MB-231 cells is majorly impacted by the fluctuation of the microtubules. On the contrary, in less metastatic MDA-MB-468 TNBC cells, particle transport more depends on ATP and mainly hindered by actin network, which is denser and more closely packed than that in highly metastatic TNBC cells [93].

It is interesting to note here that the actin structures can polymerize, cross-link, and re-organize under stress. Actin filaments polymerize into various types of forms, such as cross-linked meshes, branched networks and bundled structures [94]. These conformation can be viewed as circuits composed of interconnected springs and dashpots, which act as mechanical elements governing

14

cell shape and motion [94, 95]. Each actin configuration exhibits distinct viscoelastic properties due to structural variations and force stimulation durations [94, 96]. For instance, in the branched network, capping proteins bridges the actin filaments to prevent them from unlimited growth for the optimum force production [94].

The effects of the repulsion forces that are generated between adjacent networks can be envisioned within the spring-dashpot system [94]. Increasing the degree of entanglement, while decreasing the mesh sizes, significantly enhances the rigidity in the branched networks. In addition, cross-linked actin meshes behave differently, depending on imposed force duration. If the stress is applied on short time-scale, the cross-linked actin structure does not have enough time to reorganize itself. Therefore, the network returns to its original state when stress is removed, exhibiting elastic behavior [94]. Instead, when the stress is imposed for longer durations, the cross-linked network starts to realign and undergo rearranging process (e.g. rotation, assisted by the crosslinkers), revealing viscoelastic properties [94]. Hence, the generalized Maxwell mechanical analog present in this study serves as an appropriate model for the characterization of viscoelastic behavior.

It is quite evident that staining patterns of actin cytoskeleton indicate that its concentration and organization are significantly different for normal and cancer cells. Spatial distributions of actin are presented in orthogonal projections shown in Fig. 7. The fluorescence intensity (a.u./volume) was much higher in normal breast cells than in both types of TNBC cells. In addition, the actin filaments were denser and thicker in healthy MCF-10A breast cells, with long and entangled fibers running across the whole cell body (Fig. 7A). The assembly of highly organized fibers in healthy breast cells also forms a rigid actin network, giving the cells high stiffness and viscosity (Figs. 6A and 6B).

Instead, both types of breast cancer cells reveal a lack of actin filaments at the apical sections and loss of organization in actin fiber orientation (Figs. 7B and 7C). The actin fibers majorly appear to be short and branched randomly in perinuclear regions with long fibers almost exclusively present at the basal sections. It is clear that the differences in modulus and viscosity measurements are attributed not only to the actin concentration, but also to its organization. There is, therefore, a clear linkage between the actin cytoskeletal structure and the viscoelastic properties in TNBC cells.

It is noteworthy that in current study, cell cytoskeletal structure under static condition is investigated while shear stress induces the actin cytoskeleton rearrangement. Under flow conditions, actin will undergo rapid cytoskeletal reorganization, forming increased amount of fibers that are randomly oriented [97]. With increased flow time, actin stress fibers start to orient and re-organized themselves along the flow direction [97].

5.4. Implications

Before closing, it is important to note that the use of the shear assay system may enable the detection of breast cancer at different stages. This can be accomplished by the *in situ* capture of

cell and cytoskeletal images during fluid flow over the cells. Such *in situ* displacements can be used to capture spatial and temporal strain variations, which can then be processed to determine the local viscoelastic properties in the nucleus and the cytoplasm. This methodology enables intracellular compartments tracking without introducing external species that may disrupt the physiological environment of the cell.

The limitations associated with the shear assay method also need to be addressed. The drawback at the moment is that DIC captures in-plane (two-dimensional) deformation while cells are three-dimensional. Therefore, the local viscoelastic properties should be further investigated and correlated to spatial distributions and variations in the cytoskeletal structures.

Also, although the cell cytoskeletal structure undergoes remodeling when cells becomes malignant, simple imaging techniques alone may not detect the effects of metastatic potential in the absence of the shear loading provided by the shear assay technique. In contrast, the larger displacements associated with fluidically-induced shear loading are much easier to detect and use for the measurement of the local underlying viscoelastic cell properties at different stages. The shear assay technique, therefore, has the potential for applications in cancer diagnosis. However, further work is needed to test the effectiveness of this method on multiple sheets of cells and tissue. These are some of the challenges for future work.

6. Summary and Concluding Remarks

In this study, a combination of shear assay experiments and confocal fluorescence microscopy technique was used to study the viscoelastic properties and the actin cytoskeletal structures of normal breast cells and TNBC cells. Significant changes in shear moduli and viscosities were observed in metastatic breast cancer compared to those in normal breast cells. These are associated with order-of-magnitude reductions in moduli and viscosities, and the loss of concentration and organization for actin filaments in the TNBC cells. The reduced levels of actin expression are consistent with the reductions observed in the moduli and viscosities. The differences between the structure and viscoelastic properties of less metastatic TNBC cells and normal breast cells are much less than those between highly metastatic TNBC cells and normal breast cells. Hence, our results suggest that cancer malignancy is directly correlated with cell viscoelasticity. They also show that the shear assay method may be used to detect TNBC with increasing accuracy, as the tumor progresses. This approach can not only differentiate cancerous cells from healthy cells, but also distinguish highly metastatic cells from less metastatic ones. Therefore, the shear assay technique has the potential to serve as a clinical tool for cancer screening via the measurement of the cell viscoelastic properties.

Conflict of Interest

There are no conflicts of interest to declare.

Acknowledgements

References

[1] G. Tomaiuolo, Biomechanical properties of red blood cells in health and disease towards microfluidics, Biomicrofluidics 8(5) (2014).

[2] G.Y.H. Lee, C.T. Lim, Biomechanics approaches to studying human diseases, Trends in Biotechnology 25(3) (2007) 111-118.

[3] G.B. Nash, C.S. Johnson, H.J. Meiselman, MECHANICAL-PROPERTIES OF OXYGENATED RED-BLOOD-CELLS IN SICKLE-CELL (HBSS) DISEASE, Blood 63(1) (1984) 73-82.

[4] M. Dao, C.T. Lim, S. Suresh, Mechanics of the human red blood cell deformed by optical tweezers, Journal of the Mechanics and Physics of Solids 51(11-12) (2003) 2259-2280.

[5] S. Suresh, Biomechanics and biophysics of cancer cells, Acta Biomaterialia 3(4) (2007) 413-438.

[6] S. Suresh, J. Spatz, J.P. Mills, A. Micoulet, M. Dao, C.T. Lim, M. Beil, T. Seufferlein, Connections between single-cell biomechanics and human disease states: gastrointestinal cancer and malaria, Acta Biomaterialia 1(1) (2005) 15-30.

[7] H. Babahosseini, A.N. Ketene, E.M. Schmelz, P.C. Roberts, M. Agah, Biomechanical profile of cancer stem-like/tumor-initiating cells derived from a progressive ovarian cancer model, Nanomedicine-Nanotechnology Biology and Medicine 10(5) (2014) 1013-1019.

[8] K. Hayashi, M. Iwata, Stiffness of cancer cells measured with an AFM indentation method, Journal of the Mechanical Behavior of Biomedical Materials 49 (2015) 105-111.

[9] S.E. Cross, Y.S. Jin, J. Tondre, R. Wong, J. Rao, J.K. Gimzewski, AFM-based analysis of human metastatic cancer cells, Nanotechnology 19(38) (2008).

[10] M. Pachenari, S.M. Seyedpour, M. Janmaleki, S.B. Shayan, S. Taranejoo, H. Hosseinkhani, Mechanical properties of cancer cytoskeleton depend on actin filaments to microtubules content: Investigating different grades of colon cancer cell lines, Journal of Biomechanics 47(2) (2014) 373-379.

[11] M.F. Coughlin, D.R. Bielenberg, G. Lenormand, M. Marinkovic, C.G. Waghorne, B.R. Zetter, J.J. Fredberg, Cytoskeletal stiffness, friction, and fluidity of cancer cell lines with different metastatic potential, Clinical & Experimental Metastasis 30(3) (2013) 237-250.

[12] A. Calzado-Martin, M. Encinar, J. Tamayo, M. Calleja, A.S. Paulo, Effect of Actin Organization on the Stiffness of Living Breast Cancer Cells Revealed by Peak-Force Modulation Atomic Force Microscopy, Acs Nano 10(3) (2016) 3365-3374.

[13] Q.S. Li, G.Y.H. Lee, C.N. Ong, C.T. Lim, AFM indentation study of breast cancer cells, Biochemical and Biophysical Research Communications 374(4) (2008) 609-613.

[14] M.E. Grady, R.J. Composto, D.M. Eckmann, Cell elasticity with altered cytoskeletal architectures across multiple cell types, Journal of the Mechanical Behavior of Biomedical Materials 61 (2016) 197-207.

[15] H.W. Hou, Q.S. Li, G.Y.H. Lee, A.P. Kumar, C.N. Ong, C.T. Lim, Deformability study of breast cancer cells using microfluidics, Biomedical Microdevices 11(3) (2009) 557-564.

[16] W.W. Xu, R. Mezencev, B. Kim, L.J. Wang, J. McDonald, T. Sulchek, Cell Stiffness Is a Biomarker of the Metastatic Potential of Ovarian Cancer Cells, Plos One 7(10) (2012).

[17] V. Swaminathan, K. Mythreye, E.T. O'Brien, A. Berchuck, G.C. Blobe, R. Superfine, Mechanical Stiffness Grades Metastatic Potential in Patient Tumor Cells and in Cancer Cell Lines, Cancer Research 71(15) (2011) 5075-5080.

[18] P. Kumar, R. Aggarwal, An overview of triple-negative breast cancer, Archives of Gynecology and Obstetrics 293(2) (2016) 247-269.

[19] G. Bianchini, J.M. Balko, I.A. Mayer, M.E. Sanders, L. Gianni, Triple-negative breast cancer: challenges and opportunities of a heterogeneous disease, Nature Reviews Clinical Oncology 13(11) (2016) 674-690.

[20] J.D. Obayemi, J. Hu, V.O. Uzonwanne, O.S. Odusanya, K. Malatesta, N. Anuku, W.O. Soboyejo, Adhesion of ligand-conjugated biosynthesized magnetite nanoparticles to triple negative breast cancer cells, J Mech Behav Biomed Mater 68 (2017) 276-286.

[21] T. Ovcaricek, S.G. Frkovic, E. Matos, B. Mozina, S. Borstnar, Triple negative breast cancer - prognostic factors and survival, Radiology and Oncology 45(1) (2011) 46-52.

[22] A. Hennigs, F. Riedel, A. Gondos, P. Sinn, P. Schirmacher, F. Marme, D. Jager, H.U. Kauczor, A. Stieber, K. Lindel, J. Debus, M. Golatta, F. Schutz, C. Sohn, J. Heil, A. Schneeweiss, Prognosis of breast cancer molecular subtypes in routine clinical care: A large prospective cohort study, Bmc Cancer 16 (2016).

[23] B.E. Dogan, L.W. Turnbull, Imaging of triple-negative breast cancer, Annals of Oncology 23 (2012) 23-29.

[24] K.M. Krizmanich-Conniff, C. Paramagul, S.K. Patterson, M.A. Helvie, M.A. Roubidoux, J.D. Myles, K. Jiang, M. Sabel, Triple Receptor-Negative Breast Cancer: Imaging and Clinical Characteristics, American Journal of Roentgenology 199(2) (2012) 458-464.

[25] M. Boisserie-Lacroix, G. Mac Grogan, M. Debled, S. Ferron, M. Asad-Syed, V. Brouste, S. Mathoulin-Pelissier, G. Hurtevent-Labrot, Radiological features of triple-negative breast cancers (73 cases), Diagnostic and interventional imaging 93(3) (2012) 183-90.

[26] J. Hu, J.D. Obayemi, K. Malatesta, A. Kosmrlj, W.O. Soboyejo, Enhanced cellular uptake of LHRH-conjugated PEG-coated magnetite nanoparticles for specific targeting of triple negative breast cancer cells, Materials science & engineering. C, Materials for biological applications 88 (2018) 32-45.

[27] J. Hu, S. Youssefian, J. Obayemi, K. Malatesta, N. Rahbar, W. Soboyejo, Investigation of adhesive interactions in the specific targeting of Triptorelin-conjugated PEG-coated magnetite nanoparticles to breast cancer cells, Acta biomaterialia 71 (2018) 363-378.

[28] K.J. Van Vliet, G. Bao, S. Suresh, The biomechanics toolbox: experimental approaches for living cells and biomolecules, Acta Materialia 51(19) (2003) 5881-5905.

[29] E. Moeendarbary, A.R. Harris, Cell mechanics: principles, practices, and prospects, Wiley Interdisciplinary Reviews-Systems Biology and Medicine 6(5) (2014) 371-388.

[30] A.N. Ketene, E.M. Schmelz, P.C. Roberts, M. Agah, The effects of cancer progression on the viscoelasticity of ovarian cell cytoskeleton structures, Nanomedicine-Nanotechnology Biology and Medicine 8(1) (2012) 93-102.

[31] N. Nguyen, Y. Shao, A. Wineman, J.P. Fu, A. Waas, Atomic force microscopy indentation and inverse analysis for non-linear viscoelastic identification of breast cancer cells, Mathematical Biosciences 277 (2016) 77-88.

[32] N. Schierbaum, J. Rheinlaender, T.E. Schaffer, Viscoelastic properties of normal and cancerous human breast cells are affected differently by contact to adjacent cells, Acta Biomaterialia 55 (2017) 239-248.

[33] B. Fabry, G.N. Maksym, R.D. Hubmayr, J.P. Butler, J.J. Fredberg, Implications of heterogeneous bead behavior on cell mechanical properties measured with magnetic twisting cytometry, Journal of Magnetism and Magnetic Materials 194(1-3) (1999) 120-125.

[34] N. Wang, D.E. Ingber, Probing transmembrane mechanical coupling and cytomechanics using magnetic twisting cytometry, Biochemistry and Cell Biology 73(7-8) (1995) 327-335.

[35] M. Puig-de-Morales, M. Grabulosa, J. Alcaraz, J. Mullol, G.N. Maksym, J.J. Fredberg, D. Navajas, Measurement of cell microrheology by magnetic twisting cytometry with frequency domain demodulation, Journal of Applied Physiology 91(3) (2001) 1152-1159.

[36] W.R. Trickey, F.P.T. Baaijens, T.A. Laursen, L.G. Alexopoulos, F. Guilak, Determination of the Poisson's ratio of the cell: recovery properties of chondrocytes after release from complete micropipette aspiration, Journal of Biomechanics 39(1) (2006) 78-87.

[37] M. Sato, M.J. Levesque, R.M. Nerem, MICROPIPETTE ASPIRATION OF CULTURED BOVINE AORTIC ENDOTHELIAL-CELLS EXPOSED TO SHEAR-STRESS, Arteriosclerosis 7(3) (1987) 276-286.

[38] R.M. Hochmuth, Micropipette aspiration of living cells, Journal of Biomechanics 33(1) (2000) 15-22.

[39] S. Nawaz, P. Sanchez, K. Bodensiek, S. Li, M. Simons, I.A.T. Schaap, Cell Visco-Elasticity Measured with AFM and Optical Trapping at Sub-Micrometer Deformations, Plos One 7(9) (2012).

[40] H. Zhang, K.K. Liu, Optical tweezers for single cells, Journal of the Royal Society Interface 5(24) (2008) 671-690.

[41] N.Q. Balaban, U.S. Schwarz, D. Riveline, P. Goichberg, G. Tzur, I. Sabanay, D. Mahalu, S. Safran, A. Bershadsky, L. Addadi, B. Geiger, Force and focal adhesion assembly: a close relationship studied using elastic micropatterned substrates, Nature Cell Biology 3(5) (2001) 466-472.

[42] N. Piacentini, A.B. Verkhovsky, C. Gabella, J.J. Meister, B. Vianay, Ultra-soft cantilevers and 3-D micro-patterned substrates for contractile bundle tension measurement in living cells, Lab on a Chip 14(14) (2014) 2539-2547.

[43] N. Wang, E. Ostuni, G.M. Whitesides, D.E. Ingber, Micropatterning tractional forces in living cells, Cell Motility and the Cytoskeleton 52(2) (2002) 97-106.

[44] D. Wirtz, Particle-Tracking Microrheology of Living Cells: Principles and Applications, Annual Review of Biophysics 38 (2009) 301-326.

[45] S. Yamada, D. Wirtz, S.C. Kuo, Mechanics of living cells measured by laser tracking microrheology, Biophysical Journal 78(4) (2000) 1736-1747.

[46] Y. Tseng, T.P. Kole, D. Wirtz, Micromechanical mapping of live cells by multiple-particle-tracking microrheology, Biophysical Journal 83(6) (2002) 3162-3176.

[47] D. Kirmizis, S. Logothetidis, Atomic force microscopy probing in the measurement of cell mechanics, International Journal of Nanomedicine 5 (2010) 137-145.

[48] K. Haase, A.E. Pelling, Investigating cell mechanics with atomic force microscopy, Journal of the Royal Society Interface 12(104) (2015).

[49] E.J.G. Peterman, F. Gittes, C.F. Schmidt, Laser-induced heating in optical traps, Biophysical Journal 84(2) (2003) 1308-1316.

[50] E. Evans, A. Yeung, APPARENT VISCOSITY AND CORTICAL TENSION OF BLOOD GRANULOCYTES DETERMINED BY MICROPIPET ASPIRATION, Biophysical Journal 56(1) (1989) 151-160.

[51] Y.F. Cao, R. Bly, W. Moore, Z. Gao, A.M. Cuitino, W. Soboyejo, Investigation of the viscoelasticity of human osteosarcoma cells using a shear assay method, Journal of Materials Research 21(8) (2006) 1922-1930.

[52] T.G. Vankooten, J.M. Schakenraad, H.C. Vandermei, H.J. Busscher, DEVELOPMENT AND USE OF A PARALLEL-PLATE FLOW CHAMBER FOR STUDYING CELLULAR ADHESION TO SOLID-SURFACES, Journal of Biomedical Materials Research 26(6) (1992) 725-738.

[53] E. Martines, K. McGhee, C. Wilkinson, A. Curtis, A parallel-plate flow chamber to study initial cell adhesion on a nanofeatured surface, Ieee Transactions on Nanobioscience 3(2) (2004) 90-95.

[54] J. Cao, S. Usami, C. Dong, Development of a side-view chamber for studying cell-surface adhesion under flow conditions, Annals of Biomedical Engineering 25(3) (1997) 573-580.

[55] R. Giavazzi, M. Foppolo, R. Dossi, A. Remuzzi, ROLLING AND ADHESION OF HUMAN TUMOR-CELLS ON VASCULAR ENDOTHELIUM UNDER PHYSIOLOGICAL FLOW CONDITIONS, Journal of Clinical Investigation 92(6) (1993) 3038-3044.

[56] E.M. Hetrick, M.H. Schoenfisch, Antibacterial nitric oxide-releasing xerogels: Cell viability and parallel plate flow cell adhesion studies, Biomaterials 28(11) (2007) 1948-1956.

[57] B.B. Yellen, Z.G. Forbes, D.S. Halverson, G. Fridman, K.A. Barbee, M. Chorny, R. Levy, G. Friedman, Targeted drug delivery to magnetic implants for therapeutic applications, Journal of Magnetism and Magnetic Materials 293(1) (2005) 647-654.

[58] S. Sugiura, J. Edahiro, K. Kikuchi, K. Sumaru, T. Kanamori, Pressure-driven perfusion culture microchamber array for a parallel drug cytotoxicity assay, Biotechnology and Bioengineering 100(6) (2008) 1156-1165.

[59] Y. Geng, P. Dalhaimer, S.S. Cai, R. Tsai, M. Tewari, T. Minko, D.E. Discher, Shape effects of filaments versus spherical particles in flow and drug delivery, Nature Nanotechnology 2(4) (2007) 249-255.

[60] C.A. Reinhart-King, K. Fujiwara, B.C. Berk, Physiologic stress-mediated signaling in the endothelium, Angiogenesis: in Vitro Systems 443 (2008) 25-44.

[61] T.J. Vaughan, M.G. Haugh, L.M. McNamara, A fluid-structure interaction model to characterize bone cell stimulation in parallel-plate flow chamber systems, Journal of the Royal Society Interface 10(81) (2013).

[62] D.A. Fletcher, D. Mullins, Cell mechanics and the cytoskeleton, Nature 463(7280) (2010) 485-492.

[63] L. Lu, S.J. Oswald, H. Ngu, F.C.P. Yin, Mechanical Properties of Actin Stress Fibers in Living Cells, Biophysical Journal 95(12) (2008) 6060-6071.

[64] N. Gavara, R. Chadwick, Relationship between cell stiffness and stress fiber amount, assessed by simultaneous atomic force microscopy and live-cell fluorescence imaging, Biomechanics and Modeling in Mechanobiology 15(3) (2016) 511-523.

[65] E. Friedman, M. Verderame, S. Winawer, R. Pollack, ACTIN CYTOSKELETAL ORGANIZATION LOSS IN THE BENIGN-TO-MALIGNANT TUMOR TRANSITION IN CULTURED HUMAN COLONIC EPITHELIAL-CELLS, Cancer Research 44(7) (1984) 3040-3050.

[66] J. Katsantonis, A. Tosca, S.B. Koukouritaki, P.A. Theodoropoulos, A. Gravanis, C. Stournaras, DIFFERENCES IN THE G/TOTAL ACTIN RATIO AND MICROFILAMENT STABILITY BETWEEN NORMAL AND MALIGNANT HUMAN KERATINOCYTES, Cell Biochemistry and Function 12(4) (1994) 267-274.

[67] A. Fuhrmann, J.R. Staunton, V. Nandakumar, N. Banyai, P.C.W. Davies, R. Ros, AFM stiffness nanotomography of normal, metaplastic and dysplastic human esophageal cells, Physical Biology 8(1) (2011).

[68] R.F. Ismagilov, D. Rosmarin, P.J.A. Kenis, D.T. Chiu, W. Zhang, H.A. Stone, G.M. Whitesides, Pressure-driven laminar flow in tangential microchannels: an elastomeric microfluidic switch, Analytical Chemistry 73(19) (2001) 4682-4687.

[69] A. Burgess, S. Vigneron, E. Brioudes, J.C. Labbe, T. Lorca, A. Castro, Loss of human Greatwall results in G2 arrest and multiple mitotic defects due to deregulation of the cyclin B-Cdc2/PP2A balance, Proceedings of the National Academy of Sciences of the United States of America 107(28) (2010) 12564-12569.

[70] O. Gavet, J. Pines, Progressive Activation of CyclinB1-Cdk1 Coordinates Entry to Mitosis, Developmental Cell 18(4) (2010) 533-543.

[71] N. Oezkaya, M. Nordin, Fundamentals of biomechanics: Equilibrium, motion, and deformation, Second edition, Fundamentals of biomechanics: Equilibrium, motion, and deformation, Second edition (1999) xxi+393p-xxi+393p.

[72] M. Feric, C.P. Broedersz, C.P. Brangwynne, Soft viscoelastic properties of nuclear actin age oocytes due to gravitational creep, Scientific Reports 5 (2015).

[73] Z.Q. Sun, S.S. Guo, R. Fassler, Integrin-mediated mechanotransduction, Journal of Cell Biology 215(4) (2016) 445-456.

[74] R. Alon, M.L. Dustin, Force as a facilitator of integrin conformational changes during leukocyte arrest on blood vessels and antigen-presenting cells, Immunity 26(1) (2007) 17-27.

[75] J. Li, T.A. Springer, Integrin extension enables ultrasensitive regulation by cytoskeletal force, Proceedings of the National Academy of Sciences of the United States of America 114(18) (2017) 4685-4690.

[76] A. Chigaev, T. Buranda, D.C. Dwyer, E.R. Prossnitz, L.A. Sklar, FRET detection of cellular alpha 4-integrin conformational activation, Biophysical Journal 85(6) (2003) 3951-3962.

[77] A. Chigaev, L.A. Sklar, Overview: Assays for Studying Integrin-Dependent Cell Adhesion, Integrin and Cell Adhesion Molecules: Methods and Protocols 757 (2011) 3-14.

[78] Y. Su, W. Xia, J. Li, T. Walz, M.J. Humphries, D. Vestweber, C. Cabanas, C.F. Lu, T.A. Springer, Relating conformation to function in integrin alpha(5)beta(1), Proceedings of the National Academy of Sciences of the United States of America 113(27) (2016) E3872-E3881.

[79] X.P. Xu, E. Kim, M. Swift, J.W. Smith, N. Volkmann, D. Hanein, Three-Dimensional Structures of Full-Length, Membrane-Embedded Human alpha(IIb)beta(3) Integrin Complexes, Biophysical Journal 110(4) (2016) 798-809.

[80] Y.L. Wang, L.M. McNamara, M.B. Schaffler, S. Weinbaum, A model for the role of integrins in flow induced mechanotransduction in osteocytes, Proceedings of the National Academy of Sciences of the United States of America 104(40) (2007) 15941-15946.

[81] I. Zeidman, FATE OF CIRCULATING TUMOR CELLS .1. PASSAGE OF CELLS THROUGH CAPILLARIES, Cancer Research 21(1) (1961) 38-&.

[82] I.J. Fidler, BIOLOGICAL BEHAVIOR OF MALIGNANT-MELANOMA CELLS CORRELATED TO THEIR SURVIVAL INVIVO, Cancer Research 35(1) (1975) 218-224.

[83] C.D. Paul, P. Mistriotis, K. Konstantopoulos, Cancer cell motility: lessons from migration in confined spaces, Nature Reviews Cancer 17(2) (2017) 131-140.

[84] C. Leuschner, C.S.S.R. Kumar, W. Hansel, W. Soboyejo, J. Zhou, J. Hormes, LHRH-conjugated magnetic iron oxide nanoparticles for detection of breast cancer metastases, Breast Cancer Research and Treatment 99(2) (2006) 163-176.

[85] P. Sajeesh, A. Raj, M. Doble, A.K. Sen, Characterization and sorting of cells based on stiffness contrast in a microfluidic channel, Rsc Advances 6(78) (2016) 74704-74714.

[86] E.A. Corbin, F. Kong, C.T. Lim, W.P. King, R. Bashir, Biophysical properties of human breast cancer cells measured using silicon MEMS resonators and atomic force microscopy, Lab on a Chip 15(3) (2015) 839-847.

[87] D.B. Agus, J.F. Alexander, W. Arap, S. Ashili, J.E. Aslan, R.H. Austin, V. Backman, K.J. Bethel, R. Bonneau, W.C. Chen, C. Chen-Tanyolac, N.C. Choi, S.A. Curley, M. Dallas, D. Damania, P.C.W. Davies, P. Decuzzi, L. Dickinson, L. Estevez-Salmeron, V. Estrella, M. Ferrari, C. Fischbach, J. Foo, S.I. Fraley, C. Frantz, A. Fuhrmann, P. Gascard, R.A. Gatenby, Y. Geng, S. Gerecht, R.J. Gillies, B. Godin, W.M. Grady, A. Greenfield, C. Hemphill, B.L. Hempstead, A. Hielscher, W.D. Hillis, E.C. Holland, A. Ibrahim-Hashim, T. Jacks, R.H. Johnson, A. Joo, J.E. Katz, L. Kelbauskas, C. Kesselman, M.R. King, K. Konstantopoulos, C.M. Kraning-Rush, P. Kuhn, K. Kung, B. Kwee, J.N. Lakins, G. Lambert, D. Liao, J.D. Licht, J.T. Liphardt, L.Y. Liu, M.C. Lloyd, A. Lyubimova, P. Mallick, J. Marko, O.J.T. McCarty, D.R. Meldrum, F. Michor, S.M. Mumenthaler, V. Nandakumar, T.V. O'Halloran, S. Oh, R. Pasqualini, M.J. Paszek, K.G. Philips, C.S. Poultney, K. Rana, C.A. Reinhart-King, R. Ros, G.L. Semenza, P. Senechal, M.L. Shuler, S. Srinivasan, J.R. Staunton, Y. Stypula, H. Subramanian, T.D. Tlsty, G.W. Tormoen, Y. Tseng, A. van Oudenaarden, S.S. Verbridge, J.C. Wan, V.M. Weaver, J. Widom, C. Will, D. Wirtz, J. Wojtkowiak, P.H. Wu, N. Phys Sci Oncology Ctr, A physical sciences network characterization of non-tumorigenic and metastatic cells, Scientific Reports 3 (2013).

[88] J. Guck, S. Schinkinger, B. Lincoln, F. Wottawah, S. Ebert, M. Romeyke, D. Lenz, H.M. Erickson, R. Ananthakrishnan, D. Mitchell, J. Kas, S. Ulvick, C. Bilby, Optical deformability as an inherent cell marker for testing malignant transformation and metastatic competence, Biophysical Journal 88(5) (2005) 3689-3698.

[89] C. Rotsch, M. Radmacher, Drug-induced changes of cytoskeletal structure and mechanics in fibroblasts: An atomic force microscopy study, Biophysical Journal 78(1) (2000) 520-535.

[90] T.P. Stossel, CONTRIBUTION OF ACTIN TO THE STRUCTURE OF THE CYTOPLASMIC MATRIX, Journal of Cell Biology 99(1) (1984) S15-S21.

[91] R. Ananthakrishnan, J. Guck, F. Wottawah, S. Schinkinger, B. Lincoln, M. Romeyke, T. Moon, J. Kas, Quantifying the contribution of actin networks to the elastic strength of fibroblasts, Journal of Theoretical Biology 242(2) (2006) 502-516.

[92] M. Nikkhah, J.S. Strobl, R. De Vita, M. Agah, The cytoskeletal organization of breast carcinoma and fibroblast cells inside three dimensional (3-D) isotropic silicon microstructures, Biomaterials 31(16) (2010) 4552-4561.

[93] D. Goldstein, T. Elhanan, M. Aronovitch, D. Weihs, Origin of active transport in breast-cancer cells, Soft Matter 9(29) (2013) 7167-7173.

[94] L. Blanchoin, R. Boujemaa-Paterski, C. Sykes, J. Plastino, ACTIN DYNAMICS, ARCHITECTURE, AND MECHANICS IN CELL MOTILITY, Physiological Reviews 94(1) (2014) 235-263.

[95] J. Stricker, T. Falzone, M.L. Gardel, Mechanics of the F-actin cytoskeleton, Journal of Biomechanics 43(1) (2010) 9-14.

[96] M.L. Gardel, J.H. Shin, F.C. MacKintosh, L. Mahadevan, P. Matsudaira, D.A. Weitz, Elastic Behavior of cross-linked and bundled actin networks, Science 304(5675) (2004) 1301-1305.

[97] K.G. Birukov, A.A. Birukova, S.M. Dudek, A.D. Verin, M.T. Crow, X. Zhan, N. DePaola, J.G.N. Garcia, Shear stress-mediated cytoskeletal remodeling and cortactin translocation in pulmonary endothelial cells, American Journal of Respiratory Cell and Molecular Biology 26(4) (2002) 453-464.
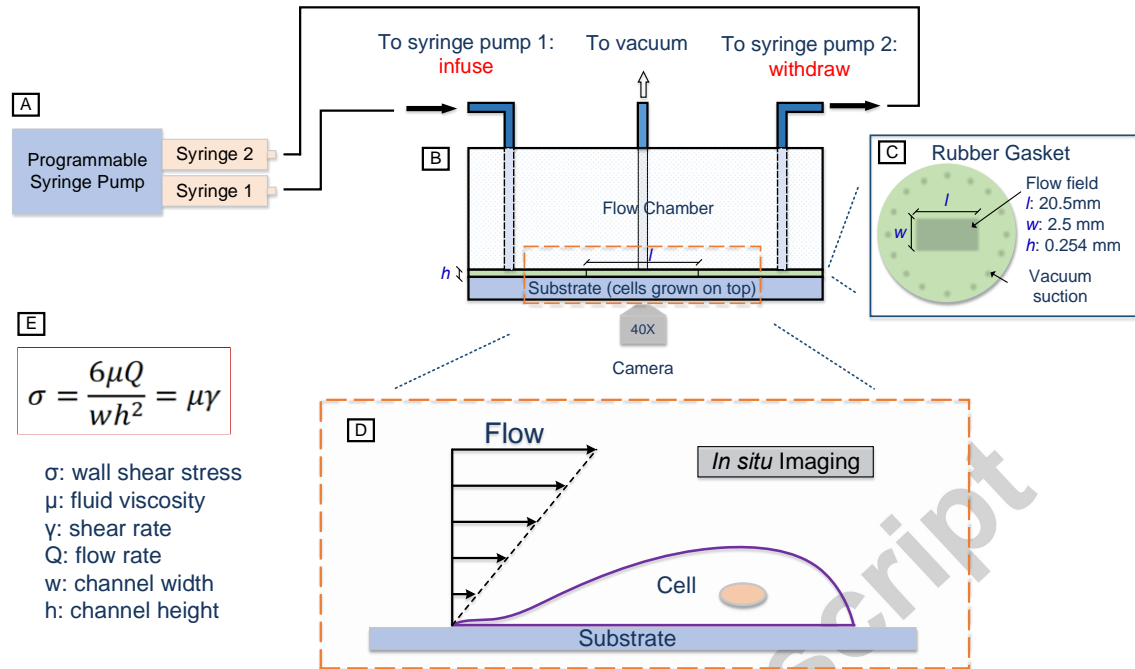
Figure 1. Schematics of shear assay system setup: (A) the programmable syringe pump delivers continuous flow to (B) the parallel flow chamber, which is monitored *in situ* by optical microscope for cell activity under fluid. A rubber gasket (C) is used to create the rectangular flow path to (D) generate laminar flow, which the cells are subject to. The wall shear stress can be estimated from the equation shown in (E).
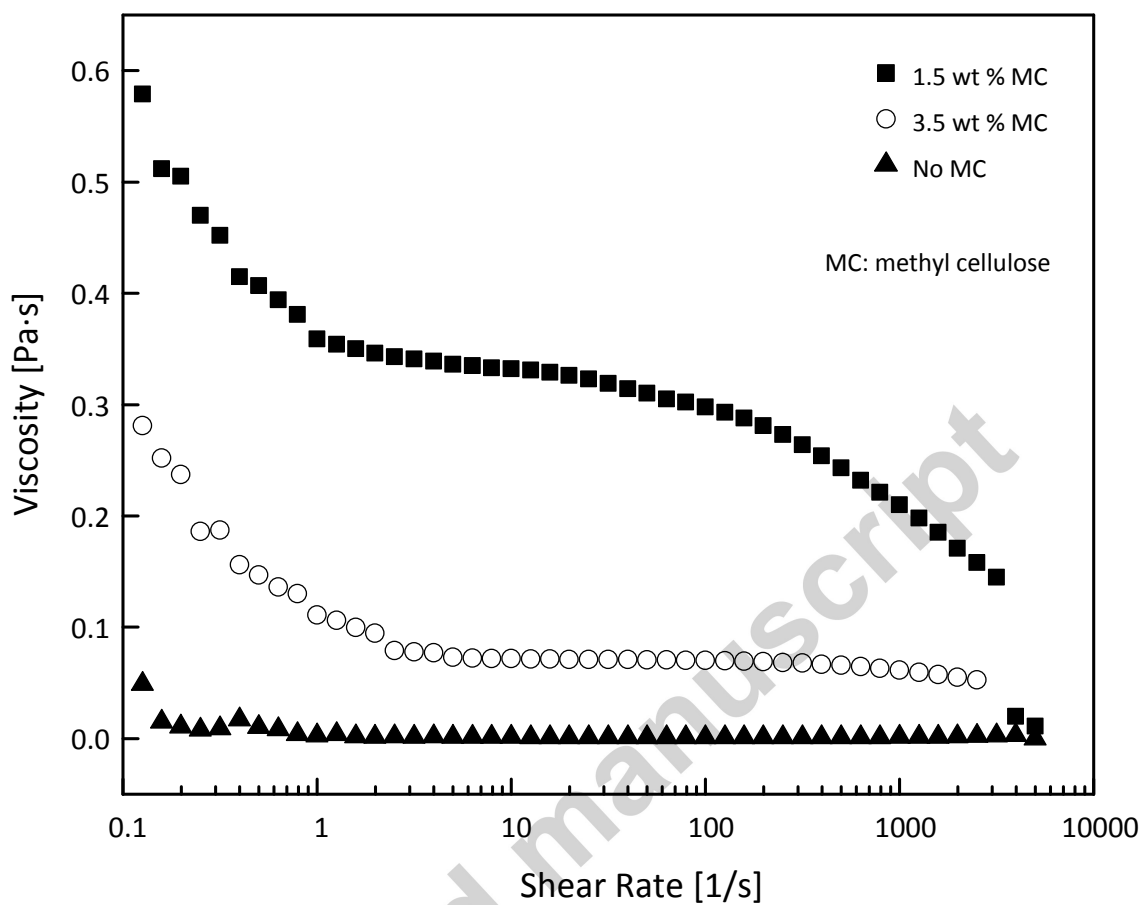
Figure 2. The viscosity of flow media that contains methylcellulose shows shear thinning behavior.

Viscoelastic Model

Fitting (primary regime only):

$$\varepsilon = \frac{\sigma}{E}[1 - \exp(-\frac{t}{\tau})] + \frac{\sigma}{\eta_1} t$$

Relaxation time: $\tau = \dfrac{\eta_2}{E}$
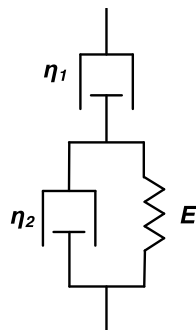
Figure 3. The three-element generalized Maxwell viscoelastic model.
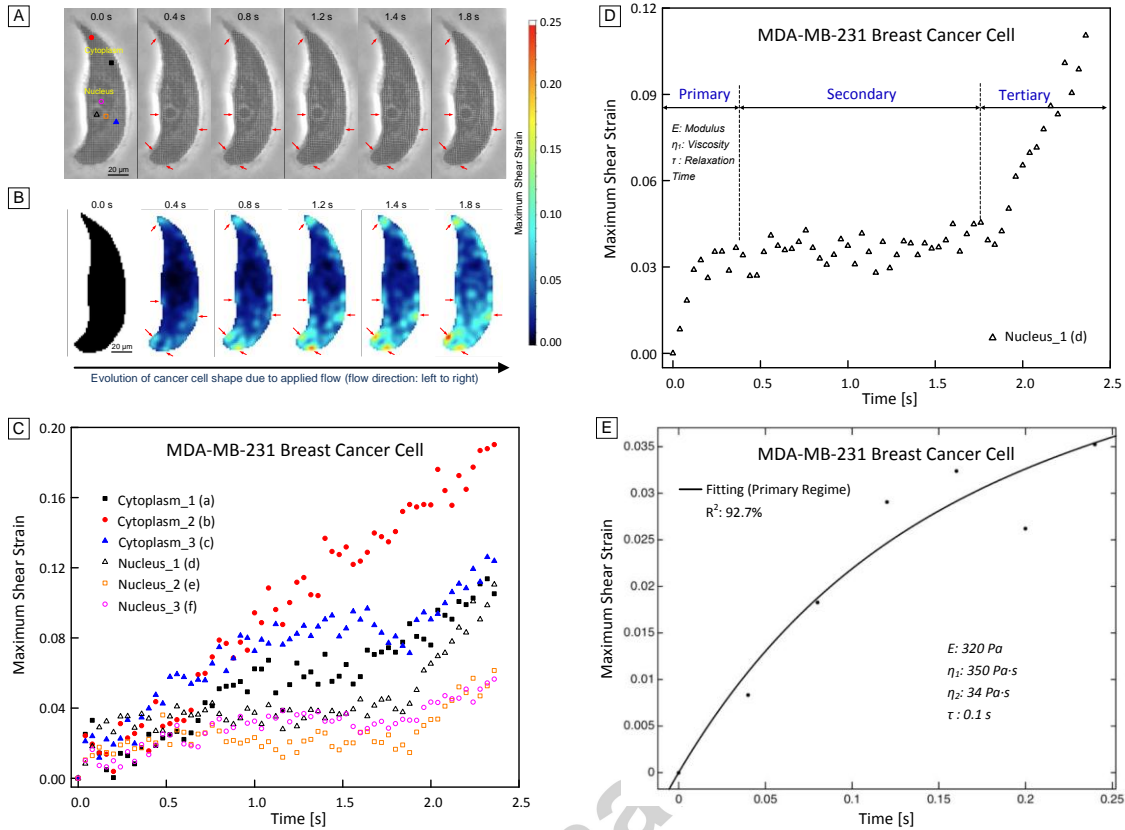
Figure 4. A representative set of strain evolution obtained using digital image correlation (DIC) technique shows the deformation of a highly metastatic MDA-MB-231 TNBC cell under applied flow ($\sigma = 10\ Pa$). The (A) grids show deformation while the (B) colors represent local strain. (C) The creep behavior in cells (both nucleus and cytoplasm regimes) in the same MDA-MB-231 breast cancer cell. (D) The three-stage creep process in nucleus is studied using the three-element viscoelastic model. (E) Fitting of the primary deformation regime in nucleus. The specific plotted locations (three each for nucleus and cytoplasm) are illustrated in image A. Red arrows point the areas with significant deformation.
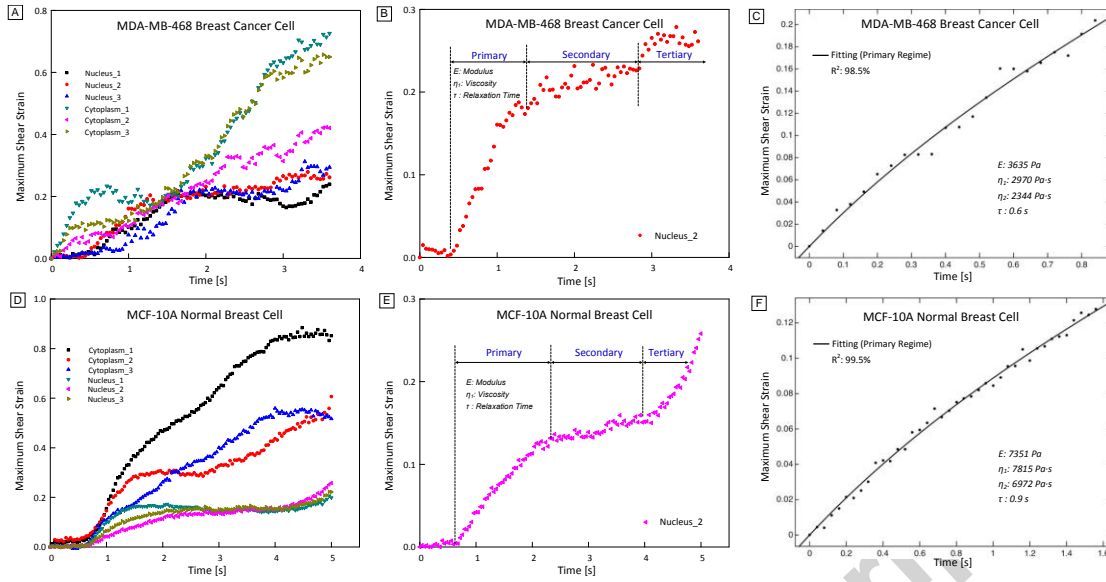
Figure 5. (A) A representative plot of the creep behavior in a less metastatic MDA-MB-468 TNBC cell (both nucleus and cytoplasm regimes); (B) three-stage creep process in nucleus; and (C) Fitting of the primary deformation regime in nucleus. (D) A representative plot of the creep behavior in a healthy MCF-10A breast cell (both nucleus and cytoplasm regimes); (E) three-stage creep process in nucleus; and (F) Fitting of the primary deformation regime in nucleus. Both types of cells are subject to $\sigma = 410\ Pa$.
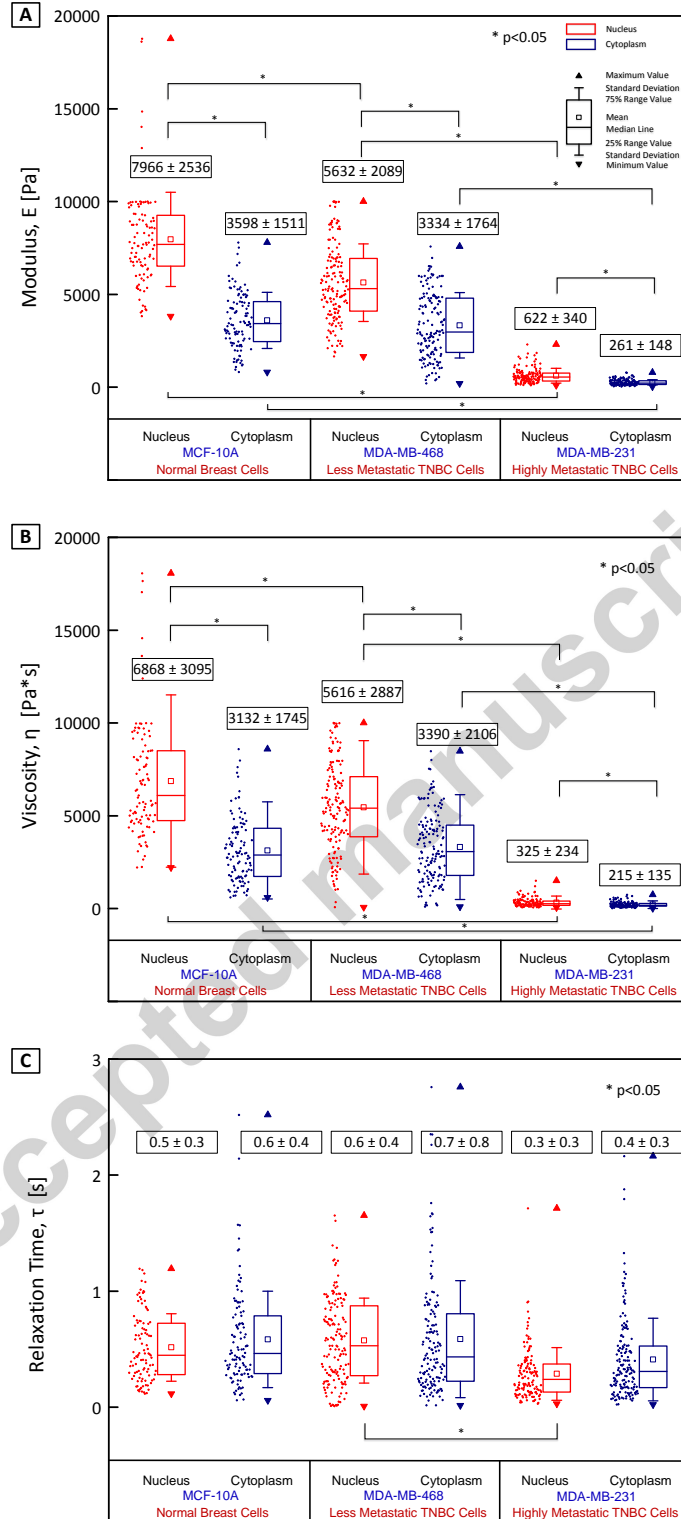
Figure 6. Summary of A: shear modulus; B: viscosity; and C: relaxation time obtained from fitting parameters for MCF-10A (normal breast cells), MDA-MB-468 (less metastatic TNBC cells) and MDA-MB-231 (highly metastatic TNBC cells) cell lines. The raw data are shown to the left to the box plot. Average, standard deviation, median, raw data and ranges of the measured data (25% to 75%) are reported.
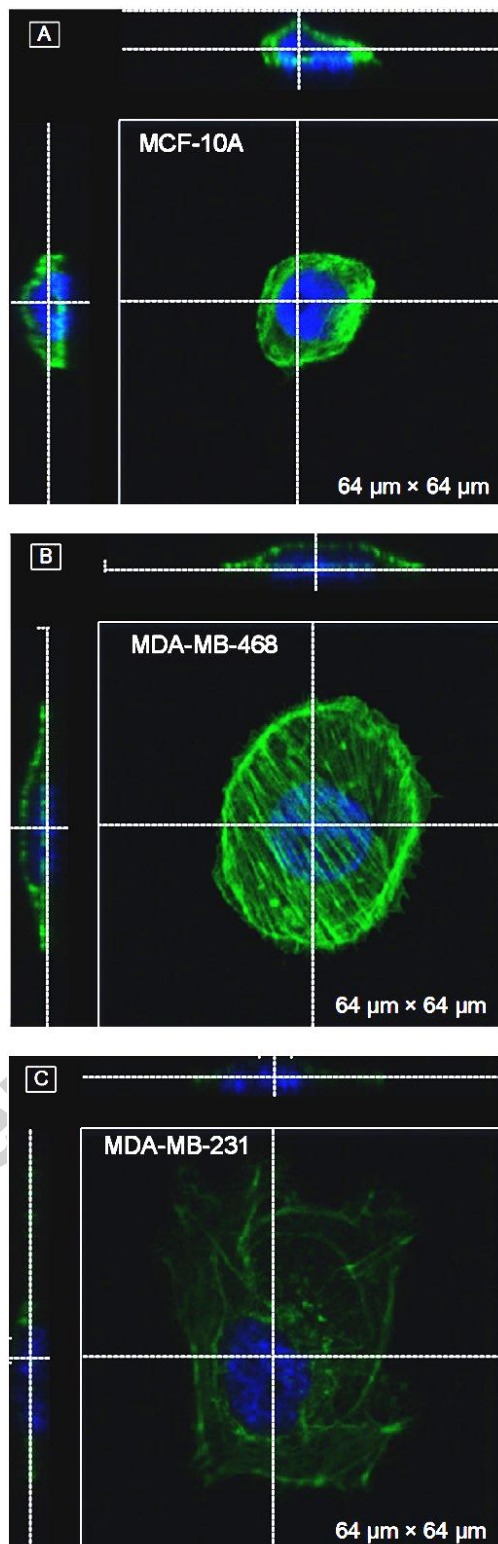
28

Figure 7. Representative confocal images of individual A: MCF-10A normal breast cell; B: MDA-MB-468 less metastatic TNBC cell; and C. MDA-MB-231 highly metastatic TNBC cell. Orthogonal views are provided to the top and left of the image. The white dashed lines indicate the positions of the orthogonal slices. Green (Phalloidin) staining reveals actin-filaments and blue (Hoechst) staining indicates nucleus. All cells were stained and imaged under same conditions.
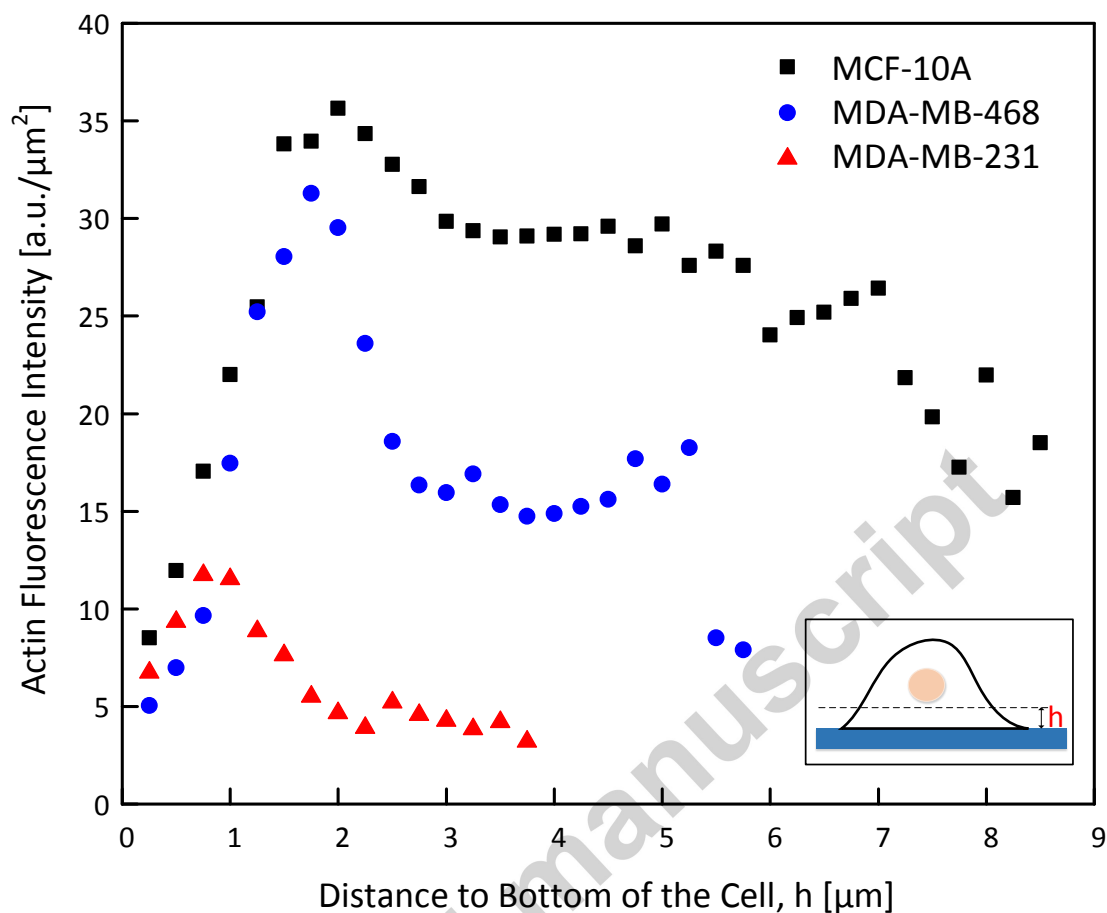
Figure 8. Representative actin fluorescence density (per unit area) at different z-heights for individual MCF-10A normal breast cell, MDA-MB-468 less metastatic TNBC cell and MDA-MB-231 highly metastatic TNBC cell, respectively.
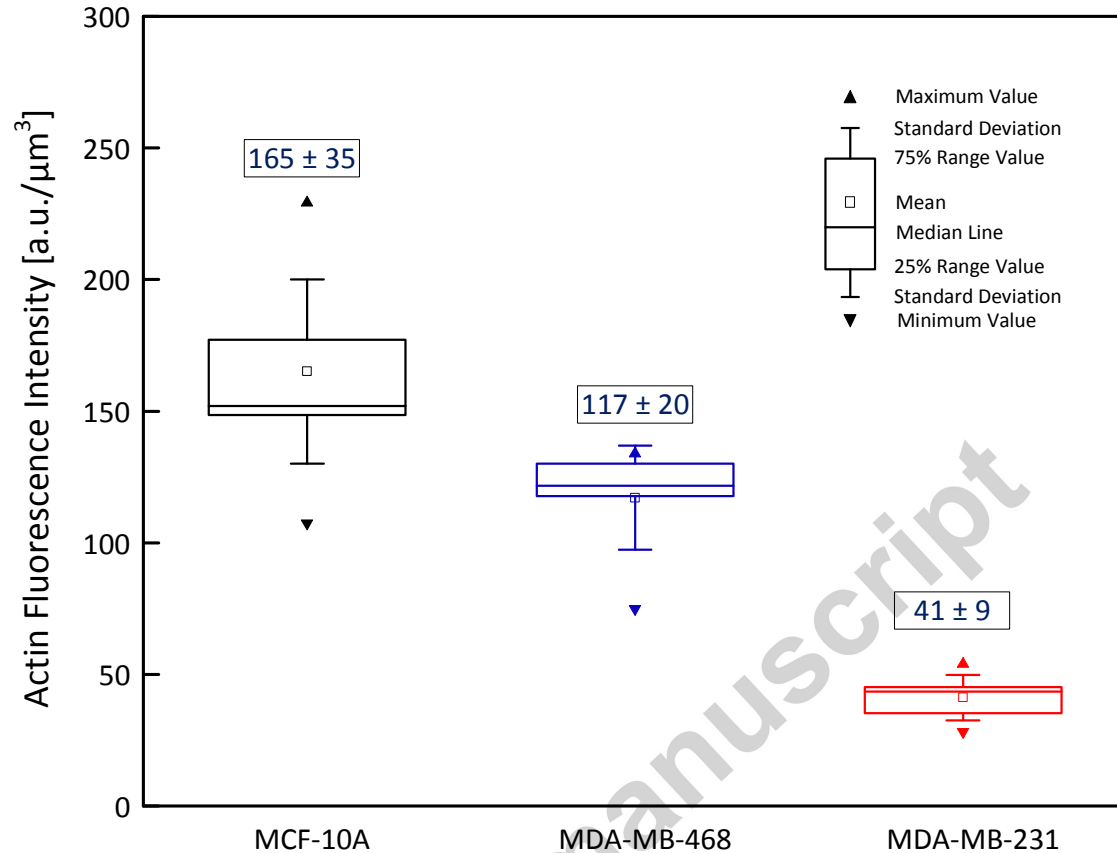
Figure 9. Summary of actin fluorescence density (per unit volume) for MCF-10A normal breast cells, MDA-MB-468 less metastatic TNBC cells and MDA-MB-231 highly metastatic TNBC cells, respectively. Average, standard deviation, median and measured data range are reported.

Highlights

- Combined shear assay and DIC method can measure local cell viscoelasticity
- TNBC cells can be differentiated from normal breast cells based on viscoelasticity
- TNBC cell viscoelasticity correlates with their actin cytoskeletal structure
- Shear assay and DIC approaches provides new insights for TNBC screening